

## High-Frequency Elastic Coupling at the Interface of van der Waals Nanolayers Imaged by Picosecond Ultrasonics

Jake D. G. Greener,<sup>†</sup> Elton de Lima Savi,<sup>‡,§</sup> Andrey V. Akimov,<sup>\*,†,§</sup> Samuel Raetz,<sup>‡,§</sup> Zakhar Kudrynskiy,<sup>†</sup> Zakhar D. Kovalyuk,<sup>§,§</sup> Nikolay Chigarev,<sup>‡</sup> Anthony Kent,<sup>†</sup> Amalia Patané,<sup>†</sup> and Vitalyi Gusev<sup>‡</sup>

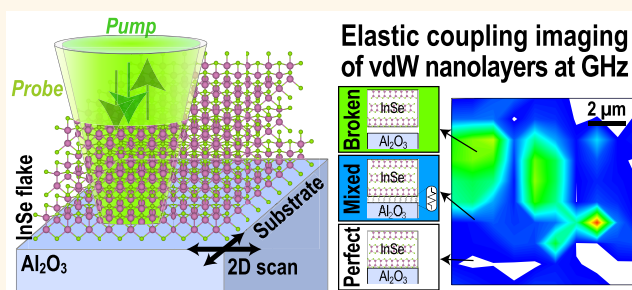
<sup>†</sup>School of Physics and Astronomy, The University Nottingham, Nottingham NG7 2RD, U.K.

<sup>‡</sup>Laboratoire d'Acoustique de l'Université du Mans, LAUM - UMR 6613 CNRS, Le Mans Université, Avenue Olivier Messiaen, 72085 Le Mans Cedex 9, France

<sup>§</sup>Chernivtsi Branch of Frantsevich Institute for Problems of Materials Science, the National Academy of Sciences of Ukraine 5, I. Vilde Street, Chernivtsi, 58001, Ukraine

**ABSTRACT:** Although the topography of van der Waals (vdW) layers and heterostructures can be imaged by scanning probe microscopy, high-frequency interface elastic properties are more difficult to assess. These can influence the stability, reliability, and performance of electronic devices that require uniform layers and interfaces. Here, we use picosecond ultrasonics to image these properties in vdW layers and heterostructures based on well-known exfoliable materials, *i.e.*, InSe, hBN, and graphene. We reveal a strong, uniform elastic coupling between vdW layers over a wide range of frequencies of up to tens of gigahertz (GHz) and in-plane areas of  $100 \mu\text{m}^2$ . In contrast, the vdW layers can be weakly coupled to their supporting substrate, behaving effectively as free-standing membranes. Our data and analysis demonstrate that picosecond ultrasonics offers opportunities to probe the high-frequency elastic coupling of vdW nanolayers and image both “perfect” and “broken” interfaces between different materials over a wide frequency range, as required for future scientific and technological developments.

**KEYWORDS:** elastic interface coupling, van der Waals nanolayers, picosecond ultrasonics, phonon imaging, coherent phonons, pump–probe technique



Two-dimensional (2D) van der Waals (vdW) layers and heterostructures have received considerable interest due to their versatile electronic, optical, and elastic properties for a wide range of potential applications.<sup>1–4</sup> In these crystals, the atoms in each vdW layer are bound together by strong covalent bonds, whereas the layers are coupled by weak vdW forces. This strong anisotropy of interatomic forces makes possible the use of a simple exfoliation-based fabrication method to realize vdW flakes as thin as one layer.<sup>5–9</sup> In particular, large-area ( $>10 \text{ cm}^2$ ) layers can now be fabricated by exploiting the adhesion properties of different materials.<sup>10</sup> Despite considerable progress in the growth of 2D vdW crystals and heterostructures,<sup>11–14</sup> the exfoliation-based fabrication method remains the most common approach to the fabrication of high-quality vdW nanolayers and heterostructures. However, it also presents some drawbacks due to random lateral size and thickness of the layers and the limited control of the quality of the interface between the layers.

A crucial requirement in the fabrication of 2D structures is their in-plane spatial homogeneity. This can be influenced not only by the uniformity of the individual layers but also by their adhesion to the substrate and/or another vdW layer. The interface between two materials can be considered ideal when the two contacting surfaces are atomically flat and, correspondingly, the force between the neighboring layers is homogeneous in the plane. In reality, the interface between two vdW layers or between a vdW layer and its supporting substrate is not elastically perfect. The strength of elastic interaction at the interface depends on the interlayer distance, which may vary in the layer plane due to defects and/or surface roughness. Also, molecular species (adsorbed water, hydrocarbons, *etc.*) in the air between a 2D crystal and a substrate

Received: June 27, 2019

Accepted: September 5, 2019

Published: September 5, 2019

can induce the formation of bubbles with a morphology determined by the vdW attraction of the layer to the substrate and the elastic energy needed to deform it. For example, stiff 2D crystals, such as graphene or monolayer hexagonal boron nitride (hBN), tend to form small, low-density bubbles and large (up to  $100 \mu\text{m}^2$ ) areas with an ideal vdW interface.<sup>15</sup>

Microscopy techniques, such as atomic force microscopy (AFM), scanning electron (SEM) and transmission electron microscopy (TEM), can probe the topography of surfaces and inhomogeneities across an interface with atomic resolution. Also, optical techniques, such as photoluminescence, photoconductivity, and Raman scattering can reveal electronic, vibrational, and optical properties with sub-micrometer spatial resolution. In particular, Raman scattering has been used to probe the interlayer coupling in vdW heterostructures<sup>16,17</sup> and to image lateral spatial inhomogeneities.<sup>18</sup> However, the elastic properties at high frequencies are generally difficult to probe. This can influence the stability, reliability and performance of electronic devices that require uniform layers and control over the charge and out-of-plane phonon transport across interfaces. For these studies *picosecond ultrasonic* imaging is ideally suited. Due to the high frequency (up to  $\sim 1$  THz) and corresponding nanometer wavelength of phonons generated by fast laser pulses, a high depth ( $\sim 0.1$  nm)<sup>19,20</sup> and lateral (down to about 100 nm) resolution<sup>19,21–23</sup> can be achieved. Previous studies have demonstrated its successful use to image various distributed inhomogeneities inside solids, polycrystalline materials, and vegetable and animal cells.<sup>24–27</sup> Imaging the adhesion between different layers inside a computer chip by monitoring the reflection amplitude of the picosecond acoustic echoes was first developed for the microelectronic industry<sup>28</sup> and more recently used to study the adhesion of biological cells.<sup>29</sup> The adhesion between particles also influences the vibrations and elasticity of nanoparticle supercrystals and colloids,<sup>30–34</sup> while the adhesion of a film/particle to the substrate influences their resonant acoustic oscillations.<sup>35–40</sup> Thus, the imaging of the adhesion of a film to the substrate could be conducted by measuring the parameters of the local resonant vibrations of the film.

Here, we demonstrate that *picosecond ultrasonics* offers opportunities to image the elastic coupling between vdW layers or a vdW layer and its supporting substrate, as required for the fabrication of new functional systems with precise control of interfacial properties. We reveal a strong, uniform elastic coupling between vdW layers over a wide range of frequencies of up to tens of gigahertz (GHz) and in-plane areas of  $100 \mu\text{m}^2$ . Also, we identify extended ( $\sim 10 \mu\text{m}^2$ ) regions of “broken” interfaces corresponding to vdW layers and heterostructures weakly coupled to the substrate and behaving as free-standing membranes over a wide range of frequencies of up to 60 GHz with a quality factor  $Q \approx 10$ . Our data rely on the generation and detection of acoustic phonon resonances in high-quality samples and the analysis of the out-of-plane phonon transport and phonon resonances by elastic equations.<sup>39</sup>

## RESULTS AND DISCUSSION

Our studies focus on InSe vdW layers and InSe-based heterostructures. The InSe vdW crystal has attracted considerable interest due to the wide tunability of its optical spectrum by the layer thickness,<sup>41,42</sup> high electron mobility in 2D field effect transistors (FETs),<sup>43,44</sup> and high photoresponsivity.<sup>45–47</sup> Here, we make picosecond ultrasonic

imaging of different InSe-based structures: (a) InSe layers on sapphire; (b) InSe/InSe homojunctions on sapphire; and (c) hBN/InSe/graphene FET heterostructures on a  $\text{SiO}_2/\text{Si}$  substrate. The three different structures enable us to examine the interface between (a) a vdW InSe layer and its supporting substrate; (b) two vdW InSe layers; and (c) different vdW layers.

The picosecond ultrasonic measurements and imaging are carried out on a picosecond acoustic microscope in reflection geometry, as shown schematically in Figure 1a. The two lasers are used as pump and probe, respectively, to generate and detect coherent phonons in the vdW layers. The detection of the elastic vibrations in the layer is governed by both the

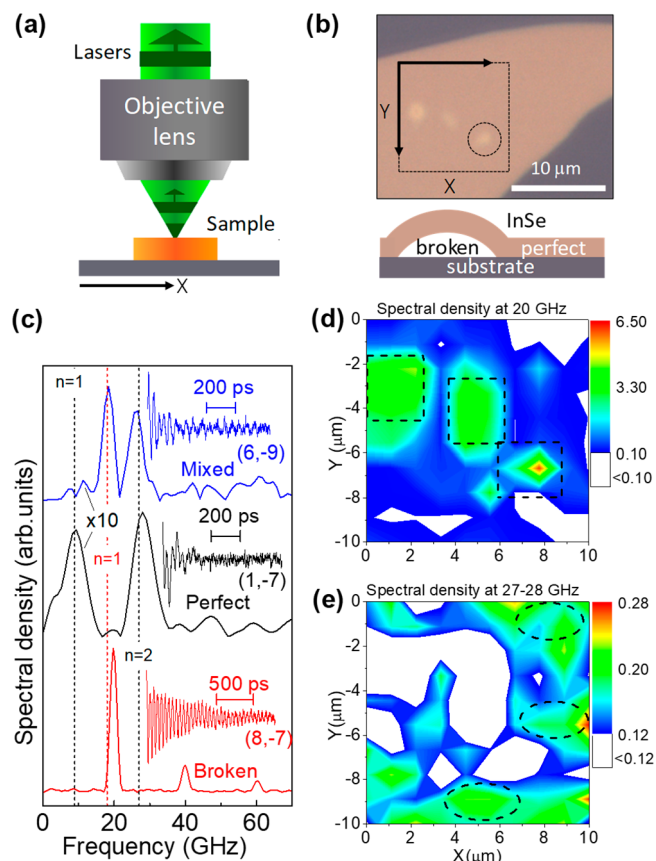


**Figure 1.** (a) Schematic of the experimental setup for picosecond ultrasonic imaging. (b) Optical image of an InSe flake on a sapphire substrate. The dotted square is the area imaged by picosecond ultrasonics, and the circle marks one of the InSe “bubbles” with no elastic contact to the substrate. Below is shown schematically broken and perfect interfaces. (c) Temporal evolutions (insets) and their fast Fourier transforms measured at three different positions with coordinates in micrometers marked in brackets. Black and red dotted lines show the calculated frequencies of the resonances for perfect and broken interfaces, respectively. The lowest red spectrum corresponds to a bubble or broken interface; the middle black spectrum corresponds to a perfect interface; the top blue spectrum corresponds to positions where both broken and perfect interfaces coexist. (d, e) Spectral density images at frequencies of 20 and 27–28 GHz corresponding to the phonon resonances for broken (d) and perfect (e) interfaces. The areas marked by dashed squares and ovals indicate homogeneous regions of broken and perfect interfaces, respectively. White areas correspond to the spectral density values below the noise level.

displacement of the layer surfaces and the photoelastic effect. To map spatially the elastic coupling between a vdW layer or heterostructure and its supporting substrate, we examine the frequency  $f_n$  and/or spectral density  $A_n$  of the acoustic phonon resonances generated in the layers. These depend on the elastic properties of the layers and can vary in the layer plane. Finally, the color maps shown below are obtained from a nearest-neighbor interpolation of data to avoid pixilation (due to discrete steps in their acquisition) and facilitate the identification of specific features.

Figure 1b shows the optical image of an InSe layer on a sapphire substrate and the specific area ( $10 \times 10 \mu\text{m}^2$ ) scanned by the pump/probe beams with  $1 \mu\text{m}$  steps along both  $x$ - and  $y$ -directions. The temporal probe signals measured at three positions and their fast Fourier transforms (FFT) are shown in the insets and main panel of Figure 1c. The three spectra in Figure 1c illustrate different cases of elastic coupling at the InSe/sapphire interface. The lowest spectrum shows three narrow lines whose frequencies agree with those of a free-standing InSe layer, as calculated from  $f_n = \frac{sn}{2a}$ , where  $s = 2500$  m/s is the sound velocity for longitudinal phonons in InSe along the direction perpendicular to the layer plane,<sup>48</sup>  $a$  is the thickness of the layer, and  $n = 1, 2, \dots$ , is the order of the harmonic resonance. The measured frequencies are reproduced with  $a = 63$  nm, close to the average value measured by AFM ( $a = 58$  nm). The middle black spectrum in Figure 1(c) has a much lower intensity, with resonance frequencies that agree well with those calculated using  $f_n = \frac{s(2n-1)}{4a}$  for an elastically perfect interface. In this case, phonons tend to propagate into the substrate, leading to a faster decay of the oscillations and broader spectral lines than for the case of a broken interface/free-standing layer. Finally, the upper spectrum in Figure 1c corresponds to the mixed case of elastic coupling with perfect and broken interfaces within the probing spot.

By measuring the phonon spectra at several positions, we can construct 2D images of the spectral density at specific frequencies. For example, Figure 1d and e show color maps of the spectral density at frequencies  $f = 20$  GHz (Figure 1d) and 27–28 GHz (Figure 1e), corresponding to the main spectral lines for broken and perfect interfaces, respectively. Red and white colors correspond to positions with maximum and minimum spectral density, respectively. It can be seen that there are extended areas of broken interfaces, as marked by dashed squares (Figure 1d). These are surrounded by regions corresponding to strong and intermediate elastic coupling.

The location of the broken interfaces correlates well with that of InSe bubbles seen in the optical (Figure 1b) and AFM (Figure 2a) images. The AFM image reveals a flake with a rough surface and three large bubbles, as also seen in the optical image of Figure 1b. Each bubble has an irregular base with an average radius  $r$  in the range 1.0 to  $1.5 \mu\text{m}$  and height  $h$  between 30 and 90 nm, corresponding to aspect ratios  $h/r = 0.04$ – $0.09$  and base angles  $\alpha = 2$ – $5^\circ$ . The Raman spectra acquired on and off the bubbles (Figure 2b) show distinctive modes peaked at 42, 116, 179, 201, and  $228 \text{ cm}^{-1}$ , corresponding to the  $E$ ,  $A_1'$ ,  $E'$ -TO/ $E''$ ,  $A_2''$ -LO, and  $A_1'$  vibrational modes of InSe, respectively. The intensity of all Raman modes tends to be slightly enhanced at the location of the bubbles [see Figure 2b and c], whereas their position does not change, indicating negligible strain.<sup>49</sup> As shown in Figure 1(c), these InSe bubbles behave as free-standing layers

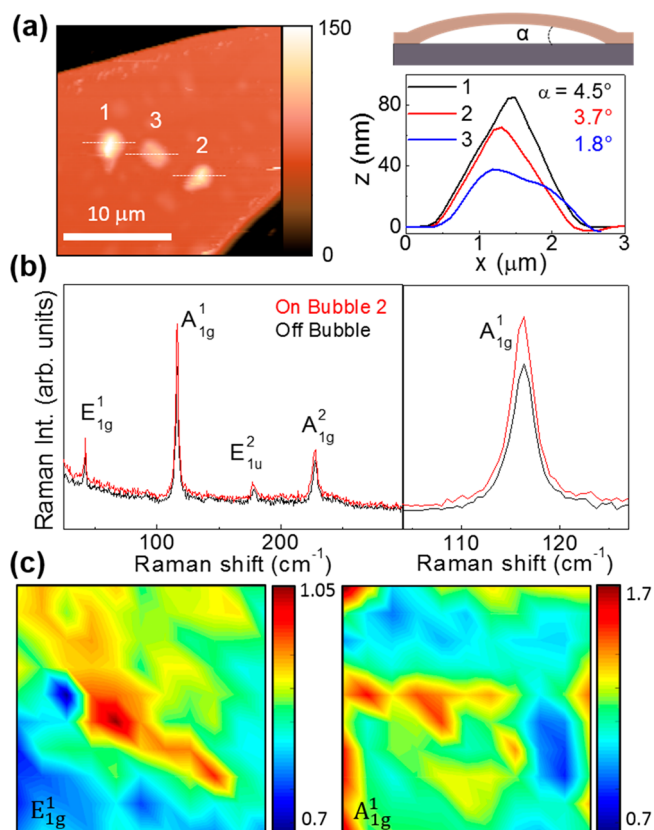
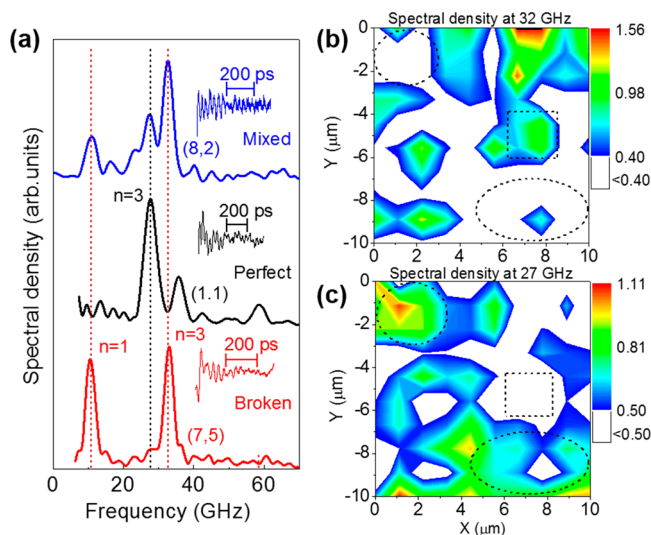


Figure 2. (a) AFM image of an InSe layer on a sapphire substrate showing three InSe “bubbles” and corresponding  $z$ -profiles along the lines shown in part (a). The base angle  $\alpha$  is calculated from the ratio between the height and width of the bubble. (b) Micro-Raman spectra on and off bubble 2 shown in part (a) ( $\lambda = 532$  nm,  $P = 0.3$  mW). (c) Raman intensity maps at  $40 \text{ cm}^{-1} E_{1g}^1$  and  $114 \text{ cm}^{-1} A_{1g}^1$ . The Raman maps are taken in the area imaged by AFM in part (a).

generating long-lived phonons (decay time  $\tau \approx 500$  ps, corresponding to a quality factor  $Q \approx 10$  for  $f = 20$  GHz) with frequencies of up to 60 GHz and  $Q \approx 30$ . We note that Raman microscopy does not reveal these acoustic phonon resonances, which would correspond to frequency shifts of less than  $2 \text{ cm}^{-1}$ .

The results for an InSe/InSe homojunction on sapphire are presented in Figure 3a. The picosecond ultrasonic spectra show phonon resonances similar to those of individual InSe layers. In this case, the structure has two interfaces: the interface between the two InSe layers and the interface between the bottom InSe layer and the sapphire substrate. Figure 3a represents temporal signals and their FFTs for three different locations of the probe spot on the homojunction. None of the peaks in the spectra correspond to independent vibrations of one of the two InSe layers, as there is a perfect elastic coupling between the layers. Thus, the vibration of the two coupled layers generates a spectrum that corresponds to a single layer with a total thickness  $a = 115$  nm. This is only slightly smaller than the sum of the base and top InSe layer thicknesses, as measured by AFM ( $a = 70 + 50 = 120$  nm).

As for the case of individual InSe flakes, the coupling of the homostructure to the substrate varies from broken to perfect. Red and black vertical dashed lines in Figure 3a correspond to selected coherent phonon resonances for broken and perfect interfaces, respectively. From the comparison of the calculated



**Figure 3.** (a) Temporal evolutions (insets) and their fast Fourier transforms measured at three different positions on an InSe/InSe homojunction on a sapphire substrate. Position coordinates inside brackets are in micrometers. The lowest red spectrum corresponds to a broken interface; the middle black spectrum corresponds to a perfect interface; the top blue spectrum corresponds to a position where both broken and perfect interfaces coexist. Black and red dotted lines show the calculated frequencies of the resonances for perfect and broken interfaces, respectively. (b, c) Spectral density images at frequencies of 32 and 27 GHz corresponding to the phonon resonances for broken (b) and perfect (c) interfaces. The areas marked by dashed squares and ovals indicate homogeneous regions of broken and perfect interfaces, respectively. White areas correspond to the spectral density values below the noise level.

and measured resonance frequencies, we assign the lower and middle spectra in Figure 3a to broken and perfect InSe/sapphire interfaces, respectively. The spectra in other locations include a larger number of lines, suggesting a mix of perfect and broken interfaces in the area of the probe spot. The assignment of the different spectra to broken and perfect interfaces is supported by images of the spectral density at specific frequencies: maxima for the spectral density at  $f = 32$  GHz (broken interface, Figure 3b) correspond to minima at  $f = 27$  GHz (perfect interface, Figure 3c) and *vice versa*. We note that similar images (not shown) are produced by mapping the spectral density of other phonon resonances within the same spectrum.

Finally, we examine the temporal pump–probe traces and corresponding FFT spectra for a hBN/InSe/graphene stack on a SiO<sub>2</sub>/Si substrate. Figure 4a and b show the optical image and representative temporal pump–probe traces and spectra at four different positions of the heterostructure: oscillations with a similar period ( $\sim 50$  ps) are clearly seen in all traces, but their decay time obtained from fitting the measured signals by decaying harmonic function varies from  $\tau = 42$  ps to  $\tau = 86$  ps. The corresponding FFT spectra in Figure 4b reveal two resonances at  $f = 18$  GHz and  $f = 32$  GHz. These values agree well with those calculated from the elastic equations<sup>39</sup> by assuming a perfect elastic coupling at the hBN/InSe interface (thickness 40 nm/40 nm) and a mixed interface between the hBN/InSe and the graphene/SiO<sub>2</sub>/Si substrate. We note that the graphene layer is not expected to have any significant effect on the phonon spectrum because of its negligible thickness.

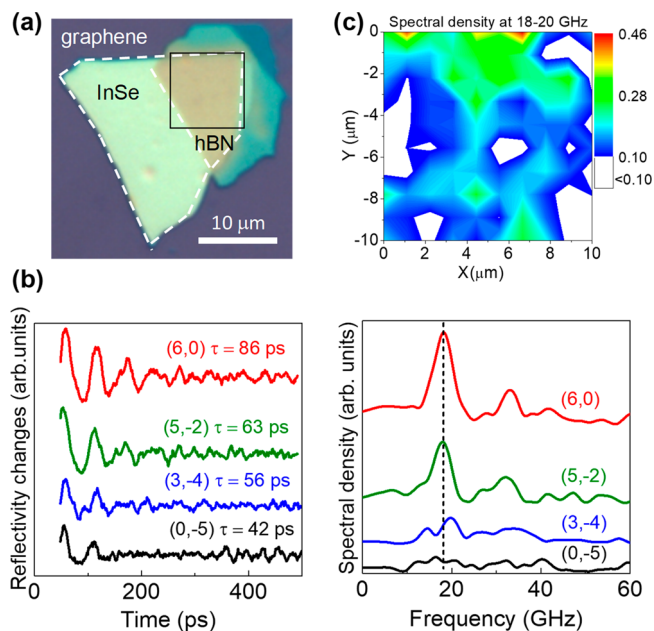


**Figure 4.** (a) Optical image of an hBN/InSe/graphene heterostructure on a SiO<sub>2</sub>/Si substrate. The black square indicates the area of the heterostructure imaged by picosecond ultrasonics in parts (b) and (c). (b) Temporal traces of reflectivity (left) and fast Fourier transforms (right) for different positions of the heterostructure. Coordinates in micrometers are indicated in brackets. Dashed vertical line indicates the main peak centered at 18 GHz. (c) Spectral density images at frequencies of 18–20 GHz. White areas correspond to the spectral density values below the noise level.

The measured resonance frequencies are almost independent of the position, but the intensity of the spectral lines varies strongly from point to point. We assign the variation in the intensity of the spectral lines and oscillation decay  $\tau$  to the non-homogeneous coupling between the hBN/InSe heterostructure and the SiO<sub>2</sub>/Si substrate. To understand it, we consider the two extreme cases of perfect and broken interfaces. We note that the acoustic impedances of InSe and SiO<sub>2</sub> have similar values. Thus, acoustic reflection at the InSe/SiO<sub>2</sub> interface is negligible (see also the discussion section). Then in the case of a perfect interface, no resonant oscillations are expected due to the fast escape of phonons from InSe to SiO<sub>2</sub>. As a result, the spectral density at the frequencies of phonon resonances is close to zero. Alternatively, in the case of a broken interface, resonant phonons are trapped in InSe, elastic vibrations have a long lifetime, and the spectral density at the resonant frequency increases.

Figure 4c shows a color map image of the spectral density at  $f = 19$  GHz. White color corresponds to the areas where the spectral density is below the noise level and correspondingly the interface is considered to be perfect. In contrast, broken regions show a longer decay time. In this case, the heterostructure behaves as a free-standing membrane with a small  $Q$ -factor ( $< 3$ ), which is significantly smaller than that ( $> 10$ ) for InSe layers or heterostructures on sapphire.

Our data and analysis demonstrate that picosecond ultrasonics can probe the high-frequency elastic coupling between different materials. In particular, whereas vdW layers tend to couple elastically over a wide range of frequencies, their coupling to a supporting substrate (e.g., sapphire or SiO<sub>2</sub>) can vary significantly in the layer plane. Quantitatively, the strength

of this elastic coupling can be described by a stiffness  $\eta$ . The stiffness  $\eta$  is defined according to Hooke's law and is used to characterize the static elastic properties, *i.e.*, the force between two contacting layers. For high-frequency properties, the impedances also become important. Thus, we introduce the parameter  $G$ , which has the dimension of a frequency and is directly related to  $\eta$ :<sup>39</sup>

$$G_{1,2} = \eta \frac{Z_1 + Z_2}{2\pi Z_1 Z_2} \quad (1)$$

where  $Z_1$  and  $Z_2$  are the acoustic impedances ( $Z = s\rho$  where  $s$  is sound velocity of longitudinal sound and  $\rho$  is the density) of the contacting materials. The  $G_{1,2}$  parameter can be compared with the frequency of the phonon resonances: the cases  $G_{1,2} \gg f$  and  $G_{1,2} \ll f$  correspond to perfect and broken interfaces, respectively.<sup>39</sup>

For individual InSe flakes or heterostructures on sapphire (Figures 1 and 3) there is a significant difference in the acoustic impedances of InSe and sapphire, *i.e.*,  $Z_{\text{sapphire}} \approx 4Z_{\text{InSe}}$ . Thus, the frequency of the phonon resonances is strongly dependent on the elastic coupling and reproduced by  $f_n = \frac{s(2n-1)}{4a}$  for  $G_{1,2} \gg f_n$  (perfect interface with  $\eta \gg 10^{18}$  N/m<sup>3</sup>) and  $f_n = \frac{sn}{2a}$  for  $G_{1,2} \ll f_n$  (broken interface with  $\eta \ll 10^{18}$  N/m<sup>3</sup>) where  $n = 1, 2, \dots$ , is the order of the harmonic resonance. The FFT spectra and images in Figure 1 show distinct regions with perfect and broken interfaces and regions where both types of resonances and interfaces coexist. Thus,  $\eta$  spans a wide range of values if compared with the values of  $\eta$  for atomically flat vdW layers ( $\eta \approx 10^{19} - 10^{20}$  N/m<sup>3</sup>).<sup>39,50</sup> Due to the strong dependence of the vdW potential energy on distance, small variations in the surface topography can result in the change of  $\eta$  and  $G_{1,2}$  by orders of magnitude. This can be clearly seen for the case in which the InSe layers form bubbles at the interface with the substrate (Figures 1 and 2). The location of the bubbles in AFM correlate closely with the location of the broken interfaces revealed by picosecond ultrasonics. Also, from the comparison of the ultrasonic image in Figure 1d with the AFM image in Figure 2a it can be seen that picosecond ultrasonics reveals areas with broken interfaces that are either larger than those shown in the AFM images or that cannot be seen in AFM, indicating a high sensitivity of picosecond acoustics to the elastic coupling of the InSe vdW layer or heterostructure to the sapphire substrate.

In contrast to the case of vdW layers on sapphire, for the hBN/InSe/graphene heterostructure on the SiO<sub>2</sub>/Si substrate the difference in acoustic impedances is small ( $Z_{\text{SiO}_2} \approx Z_{\text{InSe}}$ ). In this case, for a perfect interface of the layer with the substrate, *i.e.*,  $G_{1,2} \gg f_n$ , no phonon resonances can be generated, as shown in the lower spectrum of Figure 4b. Also, if the interface is broken or mixed, the phonon frequencies depend only weakly on  $\eta$ . However, the decay time of the oscillations,  $\tau$  (*i.e.*, the lifetime of the resonances), can be influenced by the elastic coupling, if the transmission of the energy from the film to the substrate is the dominant mechanism of the vibration attenuation. Thus, to estimate  $\eta$ , we use the relation between  $G_{1,2}$  and the phonon reflectivity  $R$  at the interface between two materials:<sup>39</sup>

$$G_{1,2} = f_n \sqrt{\frac{1 - |R|^2}{|R|^2 - R_0^2}} \quad (2)$$

where  $R_0$  is the phonon reflectivity for a perfect interface, as calculated from the acoustic mismatch theory. The phonon reflectivity  $R$  is related to the decay time  $\tau$ . For a single layer weakly coupled with the substrate we have (eq 16 in ref 39)

$$\tau = -\frac{2a}{s \ln|R|} = -\frac{1}{f_1 \ln|R|} \quad (3)$$

where  $f_1$  is the frequency of the fundamental phonon resonance. Equation 3 takes into account that the acoustic wave loses energy in each reflection at the layer/substrate interface, *i.e.*, at regular time intervals  $\Delta t = 2a/s$ , corresponding to its arrival at the layer/substrate interface. If  $a$  and  $s$  are replaced by the total thickness of the heterostructure and characteristic sound velocity, respectively, eq 3 may be used for the hBN/InSe heterostructure. We use eqs 2 and 3 to estimate the value of  $G_{1,2}$  from the measured values of  $\tau$  (42–86 ps) and by setting  $f_1 = s/2a \approx 20$  GHz. Thus, we find that  $G_{1,2}$  varies from 15 to  $\sim 100$  GHz, corresponding to values of  $\eta$  from  $10^{18}$  N/m<sup>3</sup> to  $\sim 10^{19}$  N/m<sup>3</sup>.

Equations 1–3 are directly related to the quality factor  $Q = \tau f$  of the phonon resonances. If  $\tau$  is governed mainly by the frequency-independent phonon escape to the substrate or scattering, then  $Q$  should increase with the increase of the resonance order  $n$  and corresponding value of  $f$ . Indeed, this case applies to the samples studied in this work. For instance for a single InSe layer (see Figure 1 c) the widths of the resonances at  $f = 20$  GHz ( $n = 1$ ), 40 GHz ( $n = 2$ ), and 60 GHz ( $n = 3$ ) have similar values  $\Delta f = 2.3 - 2.5$  GHz, resulting in  $Q$  increasing with  $n$  from  $Q \approx 10$  ( $n = 1$ ) to  $Q \approx 30$  ( $n = 3$ ). We also observe that  $Q$  decreases with the increase of elastic coupling at the interface with the substrate (*e.g.*, compare the middle black and the lowest red lines in Figure 1c).

## CONCLUSIONS

In summary, our studies on different samples show that areas of vdW layers mapped by picosecond ultrasonics possess an inhomogeneous elastic coupling at the interface with a sapphire or SiO<sub>2</sub>/Si substrate. In contrast, the coupling between the vdW layers can be considered as perfect for frequencies of up to several tens of GHz. The frequency, line width, and intensity of the phonons generated in the vdW layers are sensitive to the elastic properties of the layers and their elastic coupling to each other and the substrate.

The success of picosecond ultrasonic imaging in the study of vdW layers and interfaces is extremely important for identifying and sampling areas for specific studies and applications. For instance, miniaturized components for electronics and optoelectronics should possess a good elastic contact with the substrate, thus preventing overheating. Furthermore, transport of phonons across an interface affects the out-of-plane heat transfer and hence the thermal conductivity of a heterostructure, which is essential to tailor properties of thin layers for thermoelectrics and/or thermal insulation with thin coatings. The mechanical stability of the vdW heterostructures is also critical to future applications. As shown in our studies, exfoliation and dry transfer of vdW layers on specific substrates enable the fabrication of structures with homogeneous elastic properties over areas of  $\sim 10 \mu\text{m}^2$ . However, some of these regions behave as free-standing membranes. Thus, picosecond acoustics imaging could enable a nondestructive assessment of vdW layers and heterostructures for several important applications. The demonstrated

approach could also be applied to other thin films and heterostructures that absorb light.

While breakthroughs on 2D materials and heterostructures have been achieved using thin films mechanically exfoliated from bulk crystals, the controlled formation of interfaces is still in its infancy. The fabrication of functional systems requires the assembly of disparate materials with precise control of interfacial properties. This will require the development of innovative approaches for making and imaging multilayered structures for specific applications. Picosecond ultrasonics imaging, together with the fast acquisition rate offered by the ASOPS technique,<sup>51</sup> offers opportunities to map and inform the design of prospective functional systems enabling interesting avenues in science and its translation into technologies.

## METHODS

The  $\gamma$ -polytype InSe crystal is grown using the Bridgman method from a polycrystalline melt of  $\text{In}_{1.03}\text{Se}_{0.97}$ . The crystal structure is probed by X-ray diffraction using a DRON-3 X-ray diffractometer with monochromatic  $\text{Cu K}\alpha$  radiation of wavelength  $\lambda = 1.5418 \text{ \AA}$ . The InSe flakes are first mechanically exfoliated from a Bridgman-grown bulk crystal of  $\gamma$ -InSe onto a polydimethylsiloxane (PDMS) film. The PDMS/InSe film is then loaded onto a micromanipulator and transferred onto a substrate or another vdW layer. Hence the PDMS is mechanically peeled off. This process is repeated several times using InSe, hBN, and graphene to create vdW heterostructures.

We obtain the topography of the flakes by AFM and probe the optical phonon modes of the layers by Raman confocal microscopy. AFM images are acquired in the tapping mode under ambient conditions using an Asylum Research MFP-3D. The experimental setup for the Raman spectroscopy studies makes use of a doubled Nd:YVO<sub>4</sub> laser ( $\lambda = 532 \text{ nm}$ ), an  $x$ - $y$ - $z$  motorized stage, and an optical confocal microscope system equipped with a 0.5 m long monochromator with a 1200 g/mm grating. The laser beam is focused to a diameter  $d \approx 1 \mu\text{m}$  using 50 $\times$  or 100 $\times$  objectives. The Raman experiments are performed at low excitation power ( $P \leq 10^{-4} \text{ W}$ ) to avoid excessive heating. The signal is detected by a Si-charge-coupled device (CCD) camera. The Raman spectra of the InSe flakes are acquired with light polarized in the layer plane using a back scattering geometry. We use a laser excitation energy of  $h\nu = 2.33 \text{ eV}$  ( $\lambda = 532 \text{ nm}$ ) close to the energy of the interband optical transition ( $E_1' \approx 2.4 \text{ eV}$ ) between the  $p_{x,y}$ -like orbitals in the valence band and the  $s$ -like conduction band states of bulk  $\gamma$ -InSe.

The picosecond ultrasonic single-spot measurements and imaging are carried out on a picosecond acoustic microscope (JAX-M1, NETA, France)<sup>52</sup> in reflection geometry, as shown schematically in Figure 1a. Two pulsed fiber lasers with pulse duration below 200 fs and repetition rate of 42 MHz are synchronized for asynchronous optical sampling.<sup>51</sup> The two fiber lasers of wavelength  $\lambda = 517.4$  and 534.2 nm are used as pump and probe, respectively, to generate and detect coherent phonons in the vdW layers. The beams are incident close to the normal of the vdW layer and have a diameter of approximately 1.5  $\mu\text{m}$ . For the imaging experiments, the sample is mounted on a step motor  $X$ - $Y$  positioning stage with precision positioning of 0.16  $\mu\text{m}$ .

## AUTHOR INFORMATION

### Corresponding Author

\*E-mail: [andrey.akimov@nottingham.ac.uk](mailto:andrey.akimov@nottingham.ac.uk).

### ORCID

Elton de Lima Savi: 0000-0002-8680-5453

Andrey V. Akimov: 0000-0002-8173-8212

Samuel Raetz: 0000-0003-3683-8764

Zakhar D. Kovalyuk: 0000-0003-3895-4304

## Notes

The authors declare no competing financial interest.

## ACKNOWLEDGMENTS

This work was supported by the Engineering and Physical Sciences Research Council [grant number EP/M012700/1]; the European Union's Horizon 2020 research and innovation program [grant agreement number 785219]; The University of Nottingham; The National Academy of Sciences of Ukraine; and The Leverhulme Trust [RF-2017-224]. A.V.A. acknowledges the Acoustic Hub program funded by the Region Pays de la Loire (Connect Talent program) for supporting his visit to Le Mans University. We thank our colleagues from NETA who provided insight and expertise that greatly assisted the research.

## REFERENCES

- (1) Geim, A. K.; Grigorieva, I. V. Van Der Waals Heterostructures. *Nature* **2013**, *499*, 419–425.
- (2) Novoselov, K. S.; Mishchenko, A.; Carvalho, A.; Castro Neto, A. H. 2D Materials and van der Waals Heterostructures. *Science* **2016**, *353*, aac9439.
- (3) Ajayan, P.; Kim, P.; Banerjee, K. Two-Dimensional van der Waals Materials. *Phys. Today* **2016**, *69*, 38–44.
- (4) Mounet, N.; Gibertini, M.; Schwaller, P.; Campi, D.; Merkys, A.; Marrazzo, A.; Sohier, T.; Castelli, I. E.; Cepellotti, A.; Pizzi, G.; Marzari, N. Two-Dimensional Materials from High-Throughput Computational Exfoliation of Experimentally Known Compounds. *Nat. Nanotechnol.* **2018**, *13*, 246–252.
- (5) Dean, C. R.; Young, A. F.; Meric, I.; Lee, C.; Wang, L.; Sorgenfrei, S.; Watanabe, K.; Taniguchi, T.; Kim, P.; Shepard, K. L.; Hone, J. Boron Nitride Substrates for High-Quality Graphene Electronics. *Nat. Nanotechnol.* **2010**, *5*, 722–726.
- (6) Novoselov, K. S.; Geim, A. K.; Morozov, S. V.; Jiang, D.; Zhang, Y.; Dubonos, S. V.; Grigorieva, I. V.; Firsov, A. A. Electric Field Effect in Atomically Thin Carbon Films. *Science* **2004**, *306*, 666–669.
- (7) Novoselov, K. S.; Jiang, D.; Schedin, F.; Booth, T. J.; Khotkevich, V. V.; Morozov, S. V.; Geim, A. K. Two-Dimensional Atomic Crystals. *Proc. Natl. Acad. Sci. U. S. A.* **2005**, *102*, 10451–10453.
- (8) Castellanos-Gomez, A.; Buscema, M.; Molenaar, R.; Singh, V.; Janssen, L.; van der Zant, H. S.; Steele, G. A. Deterministic Transfer of Two-Dimensional Materials by All-Dry Viscoelastic Stamping. *2D Mater.* **2014**, *1*, 011002.
- (9) Masubuchi, S.; Machida, T. Classifying Optical Microscope Images of Exfoliated Graphene Flakes by Data-Driven Machine Learning. *NPJ. 2D Mater. Appl.* **2019**, *3*, 4.
- (10) Shim, J.; Bae, S. H.; Kong, W.; Lee, D.; Qiao, K.; Nezhich, D.; Park, Y. J.; Zhao, R.; Sundaram, S.; Li, X.; Yeon, H.; Choi, C.; Kum, H.; Yue, R.; Zhou, G.; Ou, Y.; Lee, K.; Mooder, J.; Zhao, X.; Ahn, J.; Hinkle, C.; Ougazzaden, A.; Kim, J. Controlled Crack Propagation for Atomic Precision Handling of Wafer-Scale Two-Dimensional Materials. *Science* **2018**, *362*, 665–670.
- (11) Li, X.; Cai, W.; An, J.; Kim, S.; Nah, J.; Yang, D.; Piner, R.; Velamakanni, A.; Jung, I.; Tutuc, E.; Banerjee, S. K.; Colombo, L.; Ruoff, R. S. Large-Area Synthesis of High-Quality and Uniform Graphene Films on Copper Foils. *Science* **2009**, *324*, 1312–1314.
- (12) Shi, Y.; Hamsen, C.; Jia, X.; Kim, K. K.; Reina, A.; Hofmann, M.; Hsu, A. L.; Zhang, K.; Li, H.; Juang, Z.; Dresselhaus, M. S.; Li, L.; Kong, J. Synthesis of Few-Layer Hexagonal Boron Nitride Thin Film by Chemical Vapor Deposition. *Nano Lett.* **2010**, *10*, 4134–4139.
- (13) Lin, K. I.; Ho, Y. H.; Liu, S. B.; Ciou, J. J.; Huang, B. T.; Chen, C.; Chang, H. C.; Tu, C. L.; Chen, C. H. Atom-Dependent Edge-Enhanced Second-Harmonic Generation on MoS<sub>2</sub> Monolayers. *Nano Lett.* **2018**, *18*, 793–797.
- (14) Chang, H. C.; Tu, C. L.; Lin, K. I.; Pu, J.; Takenobu, T.; Hsiao, C. N.; Chen, C. H. Synthesis of Large-Area InSe Monolayers by Chemical Vapor Deposition. *Small* **2018**, *14*, 1802351.

- (15) Khestanova, E.; Guinea, F.; Fumagalli, L.; Geim, A. K.; Grigorieva, I. V. Universal Shape and Pressure Inside Bubbles Appearing in van der Waals Heterostructures. *Nat. Commun.* **2016**, *7*, 12587.
- (16) Li, H.; Wu, J. B.; Ran, F.; Lin, M. L.; Liu, X. L.; Zhao, Y.; Lu, X.; Xiong, Q.; Zhang, J.; Huang, W.; Zhang, H.; Tan, P. Interfacial Interactions in Van Der Waals Heterostructures of MoS<sub>2</sub> and Graphene. *ACS Nano* **2017**, *11*, 11714–11723.
- (17) Zhang, X.; Qiao, X. F.; Shi, W.; Wu, J. B.; Jiang, D. S.; Tan, P. H. Phonon and Raman Scattering of Two-Dimensional Transition Metal Dichalcogenides from Monolayer, Multilayer to Bulk Material. *Chem. Soc. Rev.* **2015**, *44*, 2757–2785.
- (18) Su, L.; Zhang, Y.; Yu, Y.; Cao, L. Dependence of Coupling of Quasi 2-D MoS<sub>2</sub> with Substrates on Substrate Types, Probed by Temperature Dependent Raman Scattering. *Nanoscale* **2014**, *6*, 4920–4927.
- (19) Lin, K. H.; Lai, C. M.; Pan, C. C.; Chyi, J. I.; Shi, J. W.; Sun, S. Z.; Chang, C. F.; Sun, C. K. Spatial Manipulation of Nanoacoustic Waves with Nanoscale Spot Sizes. *Nat. Nanotechnol.* **2007**, *2*, 704–708.
- (20) Shen, C. C.; Weng, M. Y.; Sheu, J. K.; Yao, Y. T.; Sun, C. K. *In Situ* Monitoring of Chemical Reactions at a Solid–Water Interface by Femtosecond Acoustics. *J. Phys. Chem. Lett.* **2017**, *8*, 5430–5437.
- (21) Vertikov, A.; Kuball, M.; Nurmikko, A. V.; Maris, H. J. Time-Resolved Pump-Probe Experiments with Subwavelength Lateral Resolution. *Appl. Phys. Lett.* **1996**, *69*, 2465–2467.
- (22) Siry, P.; Belliard, L.; Perrin, B. Picosecond Acoustics with Very High Lateral Resolution. *Acta Acust. Acust.* **2003**, *89*, 925–929.
- (23) Dehoux, T.; Ishikawa, K.; Otsuka, P. H.; Tomoda, M.; Matsuda, O.; Fujiwara, M.; Takeuchi, S.; Veres, I. A.; Gusev, V.; Wright, O. B. Optical Tracking of Picosecond Coherent Phonon Pulse Focusing Inside a sub-Micron Object. *Light: Sci. Appl.* **2016**, *5*, No. e16082.
- (24) Mechri, C.; Ruello, P.; Breteau, J. M.; Baklanov, M. R.; Verdonck, P.; Gusev, V. Depth-Profiling of Elastic Inhomogeneities in Transparent Nanoporous Low-K Materials by Picosecond Ultrasonic Interferometry. *Appl. Phys. Lett.* **2009**, *95*, 091907.
- (25) Steigerwald, A.; Xu, Y.; Qi, J.; Gregory, J.; Liu, X.; Furdyna, J. K.; Varga, K.; Hmelo, A. B.; Lüpke, G.; Feldman, L. C.; Tolk, N. Semiconductor Point Defect Concentration Profiles Measured Using Coherent Acoustic Phonon Waves. *Appl. Phys. Lett.* **2009**, *94*, 111910.
- (26) Lomonosov, A. M.; Ayouch, A.; Ruello, P.; Vaudel, G.; Baklanov, M. R.; Verdonck, P.; Zhao, L.; Gusev, V. Nanoscale Noncontact Subsurface Investigations of Mechanical and Optical Properties of Nanoporous Low-K Material Thin Film. *ACS Nano* **2012**, *6*, 1410–1415.
- (27) Gusev, V.; Ruello, P. Advances In Applications of Time-Domain Brillouin Scattering for Nanoscale Imaging. *Appl. Phys. Rev.* **2018**, *5*, 031101.
- (28) Maris, H. J. Picosecond Ultrasonics. *Sci. Am.* **1998**, *278*, 86–89.
- (29) Dehoux, T.; Ghanem, M. A.; Zouani, O. F.; Rampnoux, J. M.; Guillet, Y.; Dilhaire, S.; Durrieu, M. C.; Audoin, B. All-Optical Broadband Ultrasonography of Single Cells. *Sci. Rep.* **2015**, *5*, 8650.
- (30) Courty, A.; Mermet, A.; Albouy, P. A.; Duval, E.; Pileni, M. P. Vibrational Coherence of Self-Organized Silver Nanocrystals in F.C.C. Supra-Crystals. *Nat. Mater.* **2005**, *4*, 395–398.
- (31) Gomopoulos, N.; Cheng, W.; Efremov, M.; Nealey, P. F.; Fytas, G. Out-of-Plane Longitudinal Elastic Modulus of Supported Polymer Thin Films. *Macromolecules* **2012**, *42*, 7164–7167.
- (32) Ayouch, A.; Dieudonne, X.; Vaudel, G.; Piombini, H.; Valle, K.; Gusev, V.; Belleville, P.; Ruello, P. Elasticity of an Assembly of Disordered Nanoparticles Interacting via Either van der Waals-Bonded or Covalent-Bonded Coating Layers. *ACS Nano* **2012**, *6*, 10614–10621.
- (33) Poyser, C. L.; Czerniuk, T.; Akimov, A.; Diroll, B. T.; Gauling, E.; Salasyuk, A. S.; Kent, A. J.; Yakovlev, D. R.; Bayer, B.; Murray, C. B. Coherent Acoustic Phonons in Colloidal Semiconductor Nanocrystal Superlattices. *ACS Nano* **2016**, *10*, 1163–1169.
- (34) Kim, H.; Cang, Y.; Kang, E.; Graczykowski, B.; Secchi, M.; Montagna, M.; Priestley, A. D.; Furst, E. M.; Fytas, G. Direct Observation of Polymer Surface Mobility via Nanoparticle Vibrations. *Nat. Commun.* **2018**, *9*, 2918.
- (35) Graham, H. T.; Maris, H. J.; Tauc, J. Picosecond Ultrasonics. *IEEE J. Quantum Electron.* **1989**, *25*, 2562.
- (36) Bonello, B.; Louis, G.; Battioni, P. Acoustic Investigations of the Interface Between a Metal and an Organic Compound. *Rev. Sci. Instrum.* **2003**, *74*, 889.
- (37) Pezeril, T.; Chigarev, N.; Mounier, D.; Gougeon, S.; Ruello, P.; Breteau, J. M.; Picart, P.; Gusev, V. Lumped Oscillations of a Nanofilm at Adhesion Bond. *Eur. Phys. J.: Spec. Top.* **2008**, *153*, 207–210.
- (38) Guillet, Y.; Audoin, B.; Ferrié, M.; Ravaine, S. All-Optical Ultrafast Spectroscopy of a Single Nanoparticle-Substrate Contact. *Phys. Rev. B* **2012**, *86*, 035456.
- (39) Greener, J. D. G.; Akimov, A. V.; Gusev, V.; Kudrynskiy, Z. R.; Beton, P. H.; Kovalyuk, Z. D.; Taniguchi, T.; Watanabe, K.; Kent, A. J.; Patanè, A. Coherent Acoustic Phonons in van der Waals Nanolayers and Heterostructures. *Phys. Rev. B* **2018**, *98*, 075408.
- (40) Gusev, V.; Ruello, P.; Grossman, M.; Schubert, M.; He, C.; Brick, D.; Scheer, E.; Hettich, M. Characterization of Thin-Film Adhesion and Phonon Lifetimes in Al/Si Membranes by Picosecond Ultrasonics. *New J. Phys.* **2017**, *19*, 053019.
- (41) Mudd, G. W.; Svatek, S. A.; Ren, T.; Patanè, A.; Makarovskiy, O.; Eaves, L.; Beton, P. H.; Kovalyuk, Z. D.; Lashkarev, G. D.; Kudrynskiy, Z. R.; Dmitriev, A. I. Tuning the Bandgap of Exfoliated InSe Nanosheets by Quantum Confinement. *Adv. Mater.* **2013**, *25*, 5714–5718.
- (42) Sánchez-Royo, J. F.; Muñoz-Matutano, G.; Brotons-Gisbert, M.; Martínez-Pastor, J. P.; Segura, A.; Cantarero, A.; Mata, R.; Canet-Ferrer, J.; Tobias, G.; Canadell, E.; Marqués-Hueso, J.; Gerardot, B. Electronic Structure, Optical Properties, and Lattice Dynamics in Atomically Thin Indium Selenide Flakes. *Nano Res.* **2014**, *7*, 1556–1568.
- (43) Feng, W.; Zheng, W.; Cao, W.; Hu, P. A. Back Gated Multilayer InSe Transistors with Enhanced Carrier Mobilities via the Suppression of Carrier Scattering from a Dielectric Interface. *Adv. Mater.* **2014**, *26*, 6587–6593.
- (44) Bandurin, D. A.; Tyurnina, A. V.; Geliang, L.Y.; Mishchenko, A.; Zólyomi, V.; Morozov, S. V.; Kumar, R. K.; Gorbachev, R. V.; Kudrynskiy, Z. R.; Pezzini, S.; Kovalyuk, Z. D.; Zeitler, U.; Novoselov, K. S.; Patanè, A.; Eaves, L.; Grigorieva, I. V.; Fal'ko, V. I.; Geim, A. K.; Cao, Y. High Electron Mobility, Quantum Hall Effect and Anomalous Optical Response in Atomically Thin InSe. *Nat. Nanotechnol.* **2017**, *12*, 223–227.
- (45) Tamalampudi, S.; Lu, Y.; Kumar, U. R.; Sankar, R.; Liao, C.; Moorthy, B. K.; Cheng, C.; Chou, F.; Chen, Y. High Performance and Bendable Few-Layered InSe Photodetectors with Broad Spectral Response. *Nano Lett.* **2014**, *14*, 2800–2806.
- (46) Mudd, G. W.; Svatek, S. A.; Hague, L.; Makarovskiy, O.; Kudrynskiy, Z. R.; Mellor, C. J.; Beton, P. H.; Eaves, L.; Novoselov, K. S.; Kovalyuk, Z. D.; Vdovin, E. E.; Marsden, A. J.; Wilson, N. R.; Patanè, A. High Broad-Band Photoresponsivity of Mechanically Formed InSe-Graphene van der Waals Heterostructures. *Adv. Mater.* **2015**, *27*, 3760–3766.
- (47) Yan, F.; Zhao, L.; Patanè, A.; Hu, P. A.; Wei, X.; Luo, W.; Zhang, D.; Lv, Q.; Feng, Q.; Shen, C.; Chang, K.; Eaves, L.; Wang, K. Fast, Multicolor Photodetection with Graphene-Contacted p-GaSe/n-InSe van der Waals Heterostructures. *Nanotechnology* **2017**, *28*, 27LT01.
- (48) Gatulle, M.; Fischer, M.; Chevy, A. Elastic Constants of the Layered Compounds Gas, GaSe, InSe, and their Pressure Dependence I. Experimental Part. *Phys. Status Solidi B* **1983**, *119*, 327–336.
- (49) Li, Y.; Wang, T.; Wu, M.; Cao, T.; Chen, Y.; Sankar, R.; Ulaganathan, R. K.; Chou, F.; Wetzel, C.; Xu, C. Y.; Louie, S. G.; Shi, S. Ultrasensitive Tunability of the Direct Bandgap of 2D InSe Flakes via Strain Engineering. *2D Mater.* **2018**, *5*, 021002.

(50) Björkman, T.; Gulans, A.; Krasheninnikov, A. V.; Nieminen, R. M. Van der Waals Bonding in Layered Compounds from Advanced Density-Functional First-Principles Calculations. *Phys. Rev. Lett.* **2012**, *108*, 235502.

(51) Bartels, A.; Cerna, R.; Kistner, C.; Thoma, A.; Hudert, F.; Janke, C.; Dekorsy, T. Ultrafast Time-Domain Spectroscopy Based on High-Speed Asynchronous Optical Sampling. *Rev. Sci. Instrum.* **2007**, *78*, 035107.

(52) Dilhaire, S.; Claeys, W.; Rampnoux, J. M.; Rossignol, C. Optical Heterodyne Sampling Device Having Probe and Pump Beams. <https://patentimages.storage.googleapis.com/0f/06/9d/8025f78bb9ec81/US7728317.pdf>; U.S. Patent US 007728317 B2, 2010.